

This is the accepted manuscript made available via CHORUS. The article has been published as:

# Analysis of the clustering of inertial particles in turbulent flows

Mahdi Esmaily-Moghadam and Ali Mani

Phys. Rev. Fluids **1**, 084202 — Published 20 December 2016

DOI: [10.1103/PhysRevFluids.1.084202](https://doi.org/10.1103/PhysRevFluids.1.084202)

# Analysis of the clustering of inertial particles in turbulent flows

Mahdi Esmaily-Moghadam, Ali Mani

Center for Turbulence Research, Stanford University

(Dated: November 23, 2016)

An asymptotic solution is derived for the motion of inertial particles exposed to Stokes drag in an unsteady random flow. This solution provides an estimate for the sum of Lyapunov exponents as a function of the Stokes number and Lagrangian strain- and rotation-rate autocovariance functions. The sum of exponents in a Lagrangian framework is the rate of contraction of clouds of particles and in an Eulerian framework, it is the concentration-weighted divergence of the particle velocity field. Previous literature offers an estimate of the divergence of the particle velocity field, which is applicable only in the limit of small Stokes number (R-M) (Robinson, *Comm. Pure App. Math.*, vol. 9, 1956, pp. 69-84). In addition to reproducing R-M at this limit, our analysis provides a first-order correction to R-M. Our analysis is validated by directly computed rate of contraction of clouds of particles from simulations of particles in homogeneous isotropic turbulence over a broad range of Stokes numbers. Our analysis and R-M predictions agree well with the direct computations at the limit of small Stokes numbers. At large Stokes numbers, in contrast to R-M, our model predictions remain bounded. In spite of an improvement over R-M, our analysis fails to predict the expansion of high Stokes clouds observed in the direct computations. Consistent with the general trend of particle segregation versus Stokes number, our analysis shows a maximum rate of contraction at an intermediate Stokes number of  $\mathcal{O}(1)$  and minimal rates of contraction at small and large Stokes numbers.

## I. INTRODUCTION

Inertial particles interacting with a spatially varying flow form regions of high concentration. This is known as particle clustering [1], segregation [2], or preferential concentration [3]. The prevalence of particle-laden flow in areas of physics and engineering has inspired decades of research with applications ranging from planet and cloud formation to combustion and pharmaceutical applications [4, 5].

These studies have established that clustering occurs when particles, characterized by their Stokes numbers, have a response time of order unity. At significantly higher Stokes numbers particles follow a ballistic trajectory that is independent of the flow. Particles with  $St \ll 1$  follow the fluid as tracers with a minimal relative motion that is essential to the formation of clusters. Various approaches have been adopted to relate clustering to the background flow and Stokes number. Experimental studies [4, 6–9] and numerical simulations [2, 10–16] have shown that Stokes numbers of order unity based on the Kolmogorov time scale are associated with the strongest clustering regime.

Under a particular set of conditions, such as low particle Reynolds and Knudsen numbers, high particle-to-fluid density ratio, absence of body force, negligible finite size effects, negligible particle-particle and particle-wall interactions, and low mass loading ratio, particle motion is well described in these systems by the Stokes equation

$$\ddot{\mathbf{X}}_i = \tau^{-1} \left( \mathbf{u}_i - \dot{\mathbf{X}}_i \right), \quad (1)$$

in which  $\mathbf{X}(t)$  is the position of a particle,  $t$  is time,  $(\dot{\bullet}) \equiv d(\bullet)/dt$ ,  $\mathbf{u}(\mathbf{X}, t)$  is the fluid velocity, and  $\tau$  is the particle relaxation time. Although Eq. (1) seems a simple ordinary differential equation, it exhibits a nonlinear chaotic behavior due to the dependence of its source term on  $\mathbf{X}$  [17]. For systems in which the assumptions associated with Eq. (1) are not completely valid, the Stokes number retains a large influence on clustering with a trend that is similar to the dynamics predicted by this simplified equation. Therefore, we consider Eq. (1) as the starting point to investigate the underlying physics of clustering at a more fundamental level and explicate the role of Stokes number in this process.

Multiple indices have been introduced in the literature for characterization of particle clustering [18]. Here we consider two classes of indices and describe their relationship. The first index is defined based on the rate at which nearby particles separate or approach each other. In other words, provided two particles at an initial infinitesimal distance  $\|\mathbf{r}(0)\|$ , they converge or diverge exponentially as

$$\|\mathbf{r}(t)\| = \|\mathbf{r}(0)\|e^{\lambda t}. \quad (2)$$

$\lambda$  is called the finite-time Lyapunov exponent and converges to the Lyapunov exponent in an ergodic system as  $t \rightarrow \infty$  [19]. Exponents much smaller than zero are indicative of a strong clustering regime. As discussed in details in the following section, there are three exponents ( $\lambda_1$ ,  $\lambda_2$ , and  $\lambda_3$ ) in a 3-dimensional flow that determine the rate of expansion and contraction of a cloud of particles in three orthogonal directions. Hence, these exponents are directly related to the rate of contraction of a cloud, which as discussed in [20] is connected to the particle number density and provide a measure of clustering.

The second index for characterization of clustering is based on the statistics of particle concentration field, which is experimentally measurable and less mathematically abstract. At the limit of small Stokes numbers, particle concentration field is a fractal [1]. Analytical relationships are established for different order statistics of a fractal and employed in this context for characterization of clustering [21]. For instance, the scaling exponent  $\zeta(n)$  obtained from  $m^n = D^\zeta$ , in which  $m(D)$  is the average mass of particles inside an infinitesimal sphere with diameter  $D$ , varies depending on the level of clustering. For example, clustering of randomly distributed particles in 3D toward a 2D manifold reduces  $\zeta$  from  $3n$  to  $2n$ . For a fractal concentration field,  $\zeta$  is directly related to the Lyapunov exponents and as a result to the first index described above [22, 23]. Hence, the Lyapunov exponents provide an estimate for a more experimentally-accessible clustering index and are of prime importance for characterization of particle clustering.

The divergence of particle velocity field is equal to the sum of the Lyapunov exponents (i.e.  $\lambda_1 + \lambda_2 + \lambda_3$ ) and computing it relates both indices described above to the background flow. At the limit of small Stokes numbers, an expression has been derived by Robinson 1956 [24] and Maxey 1987 [25] for the divergence of particle velocity field by taking the divergence of Eq. (1) under the assumptions  $\ddot{\mathbf{X}} \approx D\mathbf{u}/Dt$  and  $\nabla \cdot \mathbf{u} = 0$ .

This expression, which we consider for benchmarking our analysis and denote it by R-M hereafter, is

$$\overline{\nabla \cdot \dot{\mathbf{X}}} \approx -\tau \overline{\nabla \cdot (\mathbf{u} \cdot \nabla \mathbf{u})} = \tau \overline{(\|\mathbf{\Omega}\|^2 - \|\mathbf{S}\|^2)} \equiv \tau Q, \quad (3)$$

in which  $\mathbf{\Omega}$  and  $\mathbf{S}$  are the fluid rotation- and strain-rate tensors, respectively, and overline denotes averaging in time over trajectory of a particle. Note that the difference between the norm of these two tensors (here defined as  $Q$ ) corresponds to the second invariant of the velocity gradient tensor and half of the  $Q$ -criterion, which is a scalar function employed for identification of vortices in turbulent flows [26, 27]. The R-M expression explains that the most hospitable zone for clustering are those with high strain and low rotation rate that are conducive to the highest rate of contraction. Although this relation provides information about both indices through the sum of Lyapunov exponents, it is linearly proportional to  $\tau$  and fails to predict the non-monotonic behavior of Eq. (1) versus the Stokes number.

The primary objective of this study is finding a correction to R-M that not only reproduces it at the limit of small Stokes number (the regime that Eq. (3) applies to), but also applies to a wider range of Stokes numbers. With this motivation in mind, in what follows, an asymptotic solution is derived from Eq. (1) that quantifies the sum of Lyapunov exponents associated with inertial particle pairs. This solution expresses the sum of exponents as a function of Stokes number and background flow statistics, hence can be related to both indices described above.

In what follows, we consider a general representation of flow with oscillatory modes of strain and rotation acting simultaneously over all possible frequencies. We derive an eigenvalue problem with its eigenvalues and eigenvectors representing magnitude and directions of contractions, respectively. We show the dependence of this eigenvalue problem on the Stokes number, explaining how a particle may filter or resonate with different frequencies. We perform a detailed analysis of the Lagrangian autocovariance functions, which are the input to our analysis, and benchmark their response with a set of canonical flows. Finally, we present a validation of our analysis through a quantitative comparison against direct numerical simulation (DNS) of particle laden homogeneous isotropic turbulent (HIT) flow.

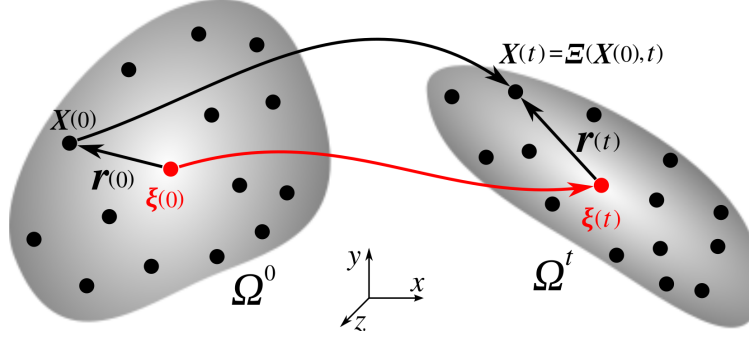


FIG. 1. Schematic of a cloud of particles,  $\Omega^t$ , defined as an infinitesimal 3D manifold occupied by a collection of particles. This cloud, which undergoes deformation characterized by  $\Xi$ , may expand or contract toward a central point  $\xi$ .

## II. ANALYTICAL DERIVATION

As the starting point, we consider a volume occupied by a collection of nearby particles, which we call a cloud. This cloud is initially denoted by  $\Omega^0$  and evolves over time with  $\Xi : \Omega^0 \rightarrow \Omega^t$  (Fig. 1). By taking function  $\Xi$  to satisfy Eq. (1),  $\Omega^t = \{X(t) \mid X(t) = \Xi(X(0), t), X(0) \in \Omega^0\}$ . By following  $\Omega^t$ , the problem is formulated on a reference frame that moves with the cloud.

Denoting the central point of the cloud by  $\xi$ , relative motion of a particle located at  $X \in \Omega^t$  to the central point is  $\mathbf{r}(t) = X(t) - \xi(t)$  (Fig. 1). Substituting this relation in Eq. (1) gives

$$\tau(\ddot{\xi}_i + \ddot{r}_i) + \dot{\xi}_i + \dot{r}_i = u_i(\xi + \mathbf{r}, t). \quad (4)$$

By bounding the size of the cloud to be much less than the Kolmogorov length scale  $\eta$ , we ensure that the size of the cloud is always less than the inertial length and as a result particles within the cloud experience a smooth linear velocity field. Hence, from the Taylor series expansion

$$u_i(\xi + \mathbf{r}, t) = u_i(\xi, t) + u_{i,j}(\xi, t)r_j + \mathcal{O}(\|\mathbf{r}\|^2), \quad (5)$$

in which  $(\bullet)_{,i} \equiv \partial(\bullet)/\partial x_i$ . Neglecting the higher order terms in Eq. (5) and using  $\tau\ddot{\xi}_i + \dot{\xi}_i = u_i(\xi, t)$  to

simplify Eq. (4) leads to

$$\tau \ddot{r}_i + \dot{r}_i = u_{i,j}(\boldsymbol{\xi}, t) r_j, \quad (6)$$

which is an exact linearized form of Eq. (1), provided  $\|\mathbf{r}\|$  is sufficiently small. Here, we have derived Eq. (6) from Eq. (1) in several steps to build physical intuition. This equation can also be obtained by taking the derivative of Eq. (1) with respect to  $\mathbf{X}(0)$  as shown in [16].

Next, we express fluid velocity in a continuous Lagrangian Fourier space that follows the cloud:

$$u_i(\boldsymbol{\xi}, t) = \sum_{\omega} \tilde{u}_i(\omega) e^{i\omega t}, \quad (7)$$

in which  $\omega = (-\infty, \infty)$ . Since finding  $\mathbf{r}$  for an individual cloud is of interest, dependence of  $\tilde{\mathbf{u}}$  on  $\boldsymbol{\xi}$  is dropped from Eq. (7). From Eqs. (7) and (6)

$$\tau \ddot{r}_i + \dot{r}_i = \sum_{\omega} \tilde{u}_{i,j}(\omega) r_j e^{i\omega t}. \quad (8)$$

These three ordinary differential equations relate particle motion to the harmonics of the velocity gradient tensor sampled along the trajectory of the cloud. One significance of this relation is that the fluid velocity gradient is characterized by the Kolmogorov scale, and thus explains our earlier use of Kolmogorov units. The appearance of the velocity gradient tensor in Eq. (8) does not imply that it only captures a subset of existing scales of the flow.  $u_{i,j}$  is a general function of time and accounts for the full turbulent spectrum, including the longer time scales of the inertial range. Additionally, due to the turbulence intermittency  $\tilde{u}_{i,j}$  can not be represented as a unique set of harmonic functions. However, as shown later in this section, it is still possible to derive a generic solution for the rate of contraction that converges statistically with sufficient sampling.

Denoting the volume of the cloud  $\Omega^t$  by  $V(\Omega^t)$ , the finite-time rate of contraction  $\mathcal{C}^t$  is defined such that

$$V(\Omega^t) = V(\Omega^0) \exp(\mathcal{C}^t t). \quad (9)$$

Based on Eq. (9), we define a time-independent rate of contraction as

$$\mathcal{C} \equiv \lim_{t \rightarrow \infty} \mathcal{C}^t. \quad (10)$$

With these definitions the cloud might rotate or even expand in a particular direction, but it contracts as long as the number density within the cloud increases. To quantify  $\mathcal{C}$ , we search for an asymptotic solution to Eq. (8) with a form of

$$r_i = e^{\lambda t} \sum_{\omega} A_i(\omega) e^{\hat{i}\omega t}, \quad (11)$$

in which  $\lambda$  and  $A_i$  are the free eigenvalues and eigenfunctions to be determined. Considering the upper bound on  $\|\mathbf{r}\|$ ,  $\lambda$  at  $t \rightarrow \infty$  is the Lyapunov exponent associated with particle pairs at  $\boldsymbol{\xi}$  and  $\boldsymbol{\xi} + \mathbf{r}$ . The form of the solution in Eq. (11) allows for oscillation over all possible frequencies,  $\omega$ , as well as contraction or expansion characterized by  $\lambda$ . Specifically, we seek contractions and expansions that persist over time scales longer than particle relaxation time and thus regimes with

$$|\lambda\tau| \ll 1, \quad (12)$$

is of particular interest.

Next, we expand our formulation at  $|\omega| < |\lambda|$  and  $|\omega| > |\lambda|$  and simplify it using Eq. (12) to obtain a 3×3 eigenvalue problem. For the sake of brevity, we use short hand notations  $\mathbf{A}^m \equiv \mathbf{A}(\omega^m)$  and  $\tilde{\mathbf{u}}^{m-n} \equiv \tilde{\mathbf{u}}(\omega^m - \omega^n)$ . Substitute Eq. (11) in (8) yields

$$\sum_{\omega^m} \left( \tau(\hat{i}\omega^m + \lambda)^2 + \hat{i}\omega^m + \lambda \right) A_i^m e^{\hat{i}\omega^m t} = \sum_{\omega^l} \sum_{\omega^n} \tilde{u}_{i,j}^l A_j^n e^{\hat{i}(\omega^l + \omega^n)t}. \quad (13)$$

Since summations are calculated over infinite intervals, we take  $\omega^l = \omega^m - \omega^n$  to simplify Eq. (13) to

$$\sum_{\omega^m} \left( \tau(\hat{i}\omega^m + \lambda)^2 + \hat{i}\omega^m + \lambda \right) A_i^m e^{\hat{i}\omega^m t} = \sum_{\omega^m} \sum_{\omega^n} \tilde{u}_{i,j}^{m-n} A_j^n e^{\hat{i}\omega^m t}, \quad (14)$$

which must hold at any  $t$ . This is achieved by ensuring

$$\left( \tau(\hat{i}\omega^m + \lambda)^2 + \hat{i}\omega^m + \lambda \right) A_i^m = \sum_{\omega^n} \tilde{u}_{i,j}^{m-n} A_j^n, \quad (15)$$

is satisfied for any  $\omega^m$ . In the following, we enforce this condition separately for small and large  $\omega^m$ .

Approximating Eq. (15) for  $|\omega^m| < |\lambda|$  yields

$$(\tau\lambda + 1) \lambda A_i^m \approx \sum_{\omega^n} \tilde{u}_{i,j}^{m-n} A_j^n, \quad (16)$$



and for  $|\omega^m| > |\lambda|$

$$\left(-\tau(\omega^m)^2 + \hat{i}\omega^m\right) A_i^m \approx \sum_{\omega^n} \tilde{u}_{i,j}^{m-n} A_j^n. \quad (17)$$

Note that  $\omega^n$  inside the summation in Eqs. (16) and (17) is not limited to small or large frequencies and covers the full spectrum of  $\tilde{u}_{i,j}$ . Rearranging Eq. (17) gives

$$A_k^n = - \sum_{\omega^l} \frac{\tau + \hat{i}/\omega^n}{1 + (\tau\omega^n)^2} \tilde{u}_{k,j}^{n-l} A_j^l, \quad (18)$$

for  $|\omega^n| > |\lambda|$ . The first term in Eq. (16) can be neglected since  $|\tau\lambda| \ll 1$  (see Eq. (12)). Therefore, substituting Eq. (18) in (16) yields

$$\lambda A_i^m = - \sum_{|\omega^n| > |\lambda|} \sum_{\omega^l} \frac{\tau + \hat{i}/\omega^n}{1 + (\tau\omega^n)^2} \tilde{u}_{i,k}^{m-n} \tilde{u}_{k,j}^{n-l} A_j^l + \sum_{|\omega^n| < |\lambda|} \sum_{\omega^l} \frac{1}{\lambda} \tilde{u}_{i,k}^{m-n} \tilde{u}_{k,j}^{n-l} A_j^l, \quad (19)$$

for  $|\omega^m| < |\lambda|$ . Since the aim of this analysis is obtaining ensemble-averaged quantities over long time periods, we neglect the terms with  $l \neq m$  in Eq. (19) ( $\tilde{u}_{i,k}^{m-n}$  and  $\tilde{u}_{i,k}^{n-l}$  are uncorrelated for  $l \neq m$ ). Hence

$$\lambda A_i^m = - \sum_{|\omega^n| > |\lambda|} \frac{\tau + \hat{i}/\omega^n}{1 + (\tau\omega^n)^2} \tilde{u}_{i,k}^{m-n} \tilde{u}_{k,j}^{n-m} A_j^m + \sum_{|\omega^n| < |\lambda|} \frac{1}{\lambda} \tilde{u}_{i,k}^{m-n} \tilde{u}_{k,j}^{n-m} A_j^m, \quad (20)$$

for  $|\omega^m| < |\lambda|$ . The velocity gradients in Eq. (20) are a function of  $|\omega^n - \omega^m|$ . Since in the first summation  $|\omega^n| > |\lambda|$  and  $|\omega^m| < |\lambda|$ , we neglect  $\omega^m$  in this summation. Additionally, the second summation is summed over a short range compared to the physical infinity, viz. of order  $\tau_\eta^{-1}$ . Hence, we neglect this term in comparison with the first summation, which is summed over a much wider range of frequencies. Our numerical results show  $|\tau_\eta\lambda| \ll 1$ . As a result Eq. (20) reduces to

$$\lambda A_i^m = - \sum_{|\omega^n| > |\lambda|} \frac{\tau + \hat{i}/\omega^n}{1 + (\tau\omega^n)^2} \tilde{u}_{i,k}^{m-n} \tilde{u}_{k,j}^n A_j^m, \quad (21)$$

for  $|\omega^m| < |\lambda|$ . In Eq. (21), the term with  $\hat{i}/\omega^n$  is an odd function of  $\omega^n$  and is canceled. Additionally, taking  $\omega = \omega^n$  yields

$$\lambda A_i^m = - \left[ \sum_{|\omega| > |\lambda|} \frac{\tau}{1 + (\tau\omega)^2} \tilde{u}_{i,k}^* \tilde{u}_{k,j} \right] A_j^m, \quad (22)$$

for  $|\omega^m| < |\lambda|$ , in which  $\tilde{\mathbf{u}}^*$  is the complex conjugate of  $\tilde{\mathbf{u}}$  and is equal to  $\tilde{\mathbf{u}}(-\omega)$ , since  $\mathbf{u} \in \mathbb{R}^3$ .

The summation in Eq. (22) includes only  $|\omega| > |\lambda|$  and hence its computation requires a prior knowledge of  $\lambda$ . To remove this dependence, we extend the summation to all frequencies by including  $|\omega| < |\lambda|$  in this summation. This change in summation bounds is in accordance with our earlier assumption in which the contribution of  $|\omega| < |\lambda|$  is negligible compared to  $|\omega| > |\lambda|$ . The contribution of these small frequencies is of the same order as the second summation in Eq. (20) that was neglected earlier. Therefore, this approximation remains within the leading order of accuracy of this analysis. Including  $|\omega| < |\lambda|$  in Eq. (22) leads to

$$\lambda A_i^m = - \left[ \sum_{\omega} \frac{\tau}{1 + (\tau\omega)^2} \tilde{u}_{i,k}^* \tilde{u}_{k,j} \right] A_j^m, \quad (23)$$

for  $|\omega^m| < |\lambda|$ . Note that the expression inside the bracket is not a function of  $\omega^m$ , indicating that  $\lambda$  is the same at small frequencies. Therefore, Eq. (23) can be written as

$$\psi \mathbf{A}^0 = \lambda \mathbf{A}^0, \quad (24)$$

in which  $\mathbf{A}^0$  is the displacement vector associated with the low frequency oscillations, i.e.  $|\omega^m| < |\lambda|$ , and

$$\psi_{ij} \equiv - \sum_{\omega} \frac{\tau}{1 + (\tau\omega)^2} \tilde{u}_{i,k}^* \tilde{u}_{k,j}. \quad (25)$$

The three eigenvectors of  $\psi$  represent the principal directions at which the cloud experiences pure contraction or expansion. The eigenvalues associated with each direction represent the rate of contraction ( $\text{real}(\lambda) < 0$ ) or expansion ( $\text{real}(\lambda) > 0$ ). Numerical investigation shows that generally one of the eigenvalues has a positive and one has a negative real part, hence most clouds expand and contract at the same time, which is consistent with previous reports [13]. The imaginary part of each eigenvalue accounts for the mean rotation.

While the instantaneous rate of expansion or contraction of a cloud is subject to oscillations due to the turbulence intermittency, the long term change of  $V(\Omega^t)$  is solely controlled by  $\lambda$  and can be computed from the product of contraction or expansion factors in the principal directions as

$$V(\Omega^t) = V(\Omega^0) \exp(\Lambda_{ii} t) \quad | \quad t \rightarrow \infty. \quad (26)$$

In this relation,  $\Lambda$  is the eigenvalue matrix of  $\psi$ , hence  $\Lambda_{ii}$  is the sum of three Lyapunov exponents  $\lambda$ 's. Considering our earlier definition of clustering index, Eq. (26) provides  $\Lambda_{ii}$  as the measure of contraction

rate for a single cloud of particles. Given that the trace is invariant,  $\Lambda_{ii}$  can be directly computed from  $\psi_{ii}$ .

Hence from Eqs. (10) and (26)

$$\mathcal{C} \approx \Lambda_{ii} = \psi_{ii} = - \sum_{\omega} \frac{\tau}{1 + (\tau\omega)^2} \tilde{u}_{i,j}^* \tilde{u}_{j,i}. \quad (27)$$

Using the convolution theorem and  $\tilde{u}_{i,j}^* \tilde{u}_{j,i} = \tilde{S}_{ij}^* \tilde{S}_{ij} - \tilde{\Omega}_{ij}^* \tilde{\Omega}_{ij}$ , Eq. (27) can be expressed in terms of a continuous integral as

$$\mathcal{C}(\tau) = \int_{-\infty}^{\infty} \frac{\tau \tilde{\rho}^Q(\omega)}{1 + (\tau\omega)^2} d\omega, \quad (28)$$

in which  $\tilde{\rho}^Q$  represents the Fourier transform of the autocovariance function  $\rho^Q$  defined as

$$\rho^Q(t) \equiv \rho^\Omega - \rho^S \equiv \overline{\Omega_{ij}(t') \Omega_{ij}(t' + t)} - \overline{S_{ij}(t') S_{ij}(t' + t)}, \quad (29)$$

with overlines denoting Lagrangian averaging over  $t'$ . Defining

$$\begin{bmatrix} \rho^I(t) \\ \rho^{II}(t) \\ \rho^{III}(t) \end{bmatrix} \equiv \begin{bmatrix} \overline{u_{1,1}(t') u_{1,1}(t' + t)} \\ \overline{u_{1,2}(t') u_{1,2}(t' + t)} \\ \overline{u_{1,2}(t') u_{2,1}(t' + t)} \end{bmatrix}, \quad (30)$$

for homogeneous and isotropic turbulence, it can be shown

$$\begin{bmatrix} \rho^\Omega(t) \\ \rho^S(t) \\ \rho^Q(t) \end{bmatrix} = 3 \begin{bmatrix} \rho^{II} - \rho^{III} \\ \rho^I + \rho^{II} + \rho^{III} \\ -\rho^I - 2\rho^{III} \end{bmatrix}. \quad (31)$$

We will analyze the behavior of these functions in the next section for HIT flow. Since these autocovariance functions are computed along the trajectory of a cloud, they are different from the Eulerian quantities and thus dependent on  $\tau$ .

Interestingly in the limit of  $St = \tau/\tau_\eta \ll 1$ , in which  $\tau_\eta$  is the Kolmogorov time scale of the flow, Eq. (28) reduces to

$$\mathcal{C} = \tau \int_{-\infty}^{\infty} \tilde{\rho}^Q d\omega = \tau \rho^Q(0) = \tau \overline{(\|\mathbf{\Omega}\|^2 - \|\mathbf{S}\|^2)} = \tau Q, \quad (32)$$

which is identical to R-M expression in Eq. (3). Note that R-M is validated in the limit of  $St < \mathcal{O}(1)$ , showing its close connection with particle clustering [28, 29]. Here using an entirely different approach, we derived a more general expression that targets a wider range of Stokes numbers. Among all flow parameters, this relation only depends on the second invariant of the velocity gradient tensor, confirming the dominant role of viscous scales on producing fluctuation in the particle concentration field [30].

Equation (28) is the most important result of this analysis, which at the first glance predicts maximum rate of contraction  $\mathcal{C}$  at intermediate  $\tau$  when  $\tilde{\rho}^Q < 0$ . Additionally, neglecting the dependence of  $\tilde{\rho}^Q$  on  $\tau$ , it predicts the decay of  $\mathcal{C}$  for  $\tau \rightarrow 0$  or  $\tau \rightarrow \infty$  proportional and inversely proportional to  $\tau$ , respectively. Furthermore, the fact that the product of  $\tau$  and  $\omega$  appeared in the denominator of Eq. (28) explains the unresponsiveness of larger particles to the fast oscillations of small flow features.

### III. DIRECT NUMERICAL SIMULATIONS

In this section, we describe the direct numerical simulations that were performed to quantify and verify the analytical results of Section II. In particular, we discuss two aspects of these simulations that are critical for a correct assessment of those results. These aspects, although generic and not specific to present analysis, are essential for reproduction of the reported results, and thus, are discussed for the sake of completeness.

We consider a triply periodic homogeneous isotropic turbulence as the background flow. To simplify collecting statistics over extended periods, we generate a stationary turbulence by continuously injecting energy into the flow via a linear forcing term that is proportional to the velocity [31]. Hence, the momentum equation is modified as

$$\rho \frac{D\mathbf{u}}{Dt} = \nabla \cdot \mathbf{T} + A\mathbf{u}, \quad (33)$$

in which  $\mathbf{T}$  is the stress tensor and  $A$  is the linear forcing term. The difficulty of this formulation is that the rate of energy supply and dissipation will not be stationary variables for a constant  $A$ . As a result, implementation of Eq. (33) with a constant  $A$  produces a time-dependent  $\tau_\eta$  with fluctuations persisting

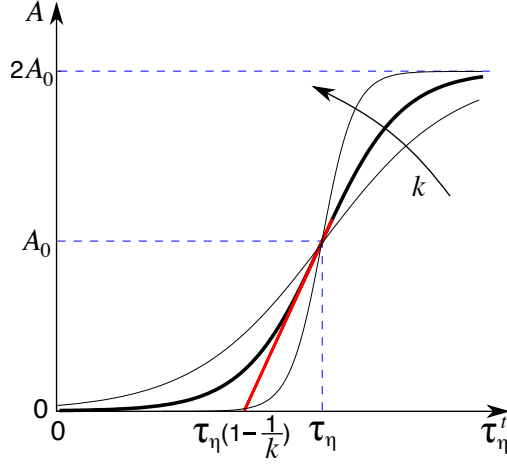


FIG. 2. The dynamic adjustment of the linear forcing coefficient  $A^t$  based on the measured  $\tau_\eta^t$  using Eq. (34).

over long periods. These fluctuations have a slow dynamics with an integral time scale that is in the order of hundreds of  $\overline{\tau_\eta}$ . Since  $\tau_\eta$  is directly related to the Stokes number of particles, a correct estimate of  $St$  relies on computing  $\tau_\eta$  such that conditions are statistically converged. However, the long integral time scale of  $\tau_\eta$  inhibits its accurate computation through a reasonable period of ensemble-averaging.

To prevent variation of global turbulence statistics several remedies have been explored [32]. Here, we developed a method that dynamically changes the linear forcing term  $A$  at each time step using

$$A^t = A \left( 1 + \tanh \left( k \left( \frac{\tau_\eta^t}{\tau_\eta} - 1 \right) \right) \right), \quad (34)$$

in which  $A$  is a baseline estimate that is computed from the target Kolmogorov time scale  $\tau_\eta$ ,  $A^t$  is dynamically changed forcing term that is implemented in the right-hand-side of Eq. (33),  $\tau_\eta^t$  is the instantaneously measured Kolmogorov time scale throughout the simulation, and  $k$  is a dimensionless control gain. This method is specifically designed to prevent variation of  $\tau_\eta$  throughout the simulation. As shown in Fig. 2, depending on the deviation of  $\tau_\eta^t$  from the target value,  $A^t$  is increased or decreased with a slope of  $kA/\tau_\eta$ . For a given box size  $L$  and fluid kinematic viscosity  $\nu$ , we choose  $A = \nu^{1/3} L^{-2/3} \tau_\eta^{-2/3}$ . This choice produces  $Re_\lambda \approx \sqrt{15}/(3A\tau_\eta)$ .

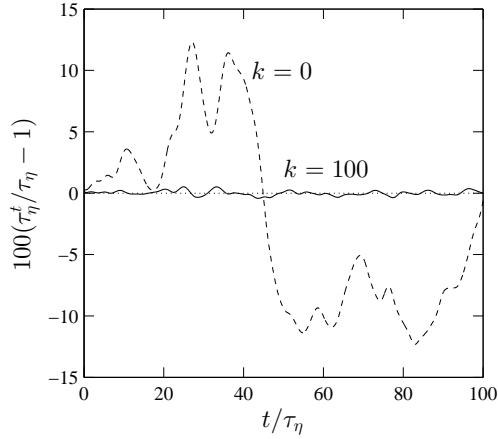


FIG. 3. Deviation of the instantaneous Kolmogorov time scale  $\tau_\eta^t$  from the target  $\tau_\eta$  in percent over the entire simulation history for controlled  $A^t$  with  $k = 100$  (solid line) and uncontrolled  $A^t$  with  $k = 0$  (dashed line).

Implementation of Eq. (34) limits the relative error in controlled  $\tau_\eta^t$  to a value that scales as  $k^{-1}$ . As shown in Fig. 3, which is obtained from a simulation at  $\text{Re}_\lambda = 26$ , controlling  $A^t$  reduces  $\sqrt{(\tau_\eta^t/\tau_\eta - 1)^2}$  from 10% to less than 0.2%. The simulation reported in the following sections is performed at  $\text{Re}_\lambda = 100$  with  $k = 100$ . In this simulation, the maximum deviation of  $\tau_\eta^t$  from the target Kolmogorov time scale is 0.3%.

The second aspect of these simulations that requires close attention is the interpolation scheme for computing quantities at the location of particles from the Eulerian grid. To accurately compute the compressibility of particle velocity field, it is essential to have an interpolation scheme that translates the incompressibility condition that is imposed on the Eulerian field to the Lagrangian field. In the other word,  $u_{i,i}(X(t); t)$  evaluated at the location of particles must be zero for incompressible flows. An interpolation scheme with an improper design will not satisfy this condition. The second issue that may arise in this context is a discontinuity in the interpolated velocity gradients along the trajectory of a particle as it crosses over Eulerian cell boundaries (Fig. 4). For example, this issue becomes apparent in the case of constructing velocity gradients from the interpolated velocities through finite-differencing. Note that increasing the order of interpolation

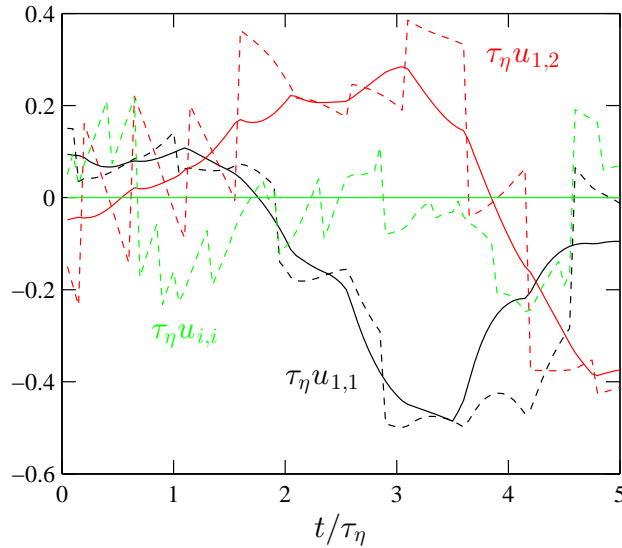


FIG. 4. The Lagrangian velocity gradients as a function of time for an arbitrary particle interpolated from an Eulerian velocity field. As a particle crosses a cell boundary, a jump is observed in the velocity gradients due to the finite-support of the interpolation scheme (dashed lines). This issue, originally caused by performing interpolation and then differentiation, is resolved by first creating a spatially-consistent  $C^0$  continuous field for the velocity gradient and then performing the Lagrangian interpolation (solid lines).

scheme (for a finite interpolation stencil) does not resolve this problem.

To prevent these two issues, we compute the velocity gradient on the Eulerian grid prior to the Eulerian-to-Lagrangian interpolation. More specifically, for a staggered uniform grid and a second order central differencing,  $u_{i,i}$  is computed on the cell center based on the velocities on the faces of the cell. For  $u_{i,j}$  and  $i \neq j$ , gradients are computed on the cell faces from the adjacent cells velocities (e.g. cell  $I + 1$  is computed based on the cells  $I$  and  $I + 2$ ). This Eulerian representation of  $u_{i,j}$  is then fed into a trilinear interpolation scheme that respects the location of Eulerian quantities on the grid while computing  $u_{i,j}$  at the location of particles. The combination of these two steps produces a  $C^0$  continuous velocity gradient as a function of time that automatically satisfies the incompressibility condition (Fig. 4).

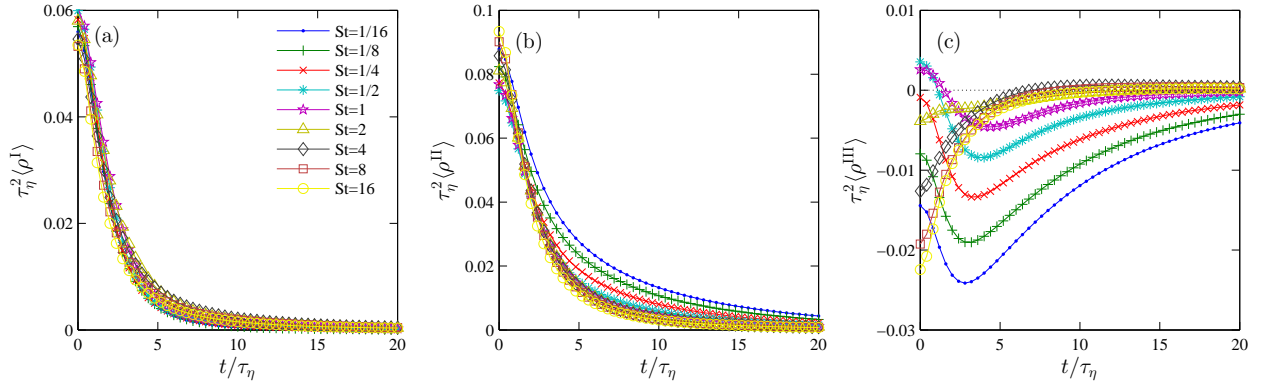


FIG. 5. The ensemble-averaged Lagrangian autocovariance functions (a)  $\langle \rho^I \rangle$ , (b)  $\langle \rho^{II} \rangle$ , and (c)  $\langle \rho^{III} \rangle$  defined in Eq. (30) at different Stokes numbers.

#### IV. ANALYSIS OF THE LAGRANGIAN AUTOCOVARIANCE FUNCTIONS

In this section, the autocovariance functions, defined in Eqs. (30) and (31), are computed for a HIT flow. DNS of a triply periodic incompressible flow at  $Re_\lambda=100$  was performed using a  $256^3$  numerical grid. Turbulence was maintained using a time varying linear forcing term (Eq. (34)). Equation (1) was solved for particles with  $St = 2^p$ ,  $p \in \{-4, \dots, 4\}$ . At each Stokes number,  $10^5$  randomly seeded particles were simulated for several large eddy turnover time to allow development of clusters. Starting from this time-evolved distribution, the velocity gradient tensor was recorded at the position of each particle for  $200\tau_\eta$  with  $0.1\tau_\eta$  intervals. The scheme described in Section III was employed for proper interpolation of the velocity gradients from the Eulerian grid to the location of particles. Having  $u_{i,j}$  as a function of time, the autocovariance functions were computed based on Eq. (30) at each St. For ensemble-averaging, denoted by  $\langle \bullet \rangle$  hereafter, this process is repeated for all particles ( $10^5$  samples at each St). The number of particles and integration period are verified to be sufficient for achieving statistical convergence. The results of these calculations are shown in Fig. 5.

To analyze the trends observed in Fig. 5, we investigate the behavior of each autocovariance function on



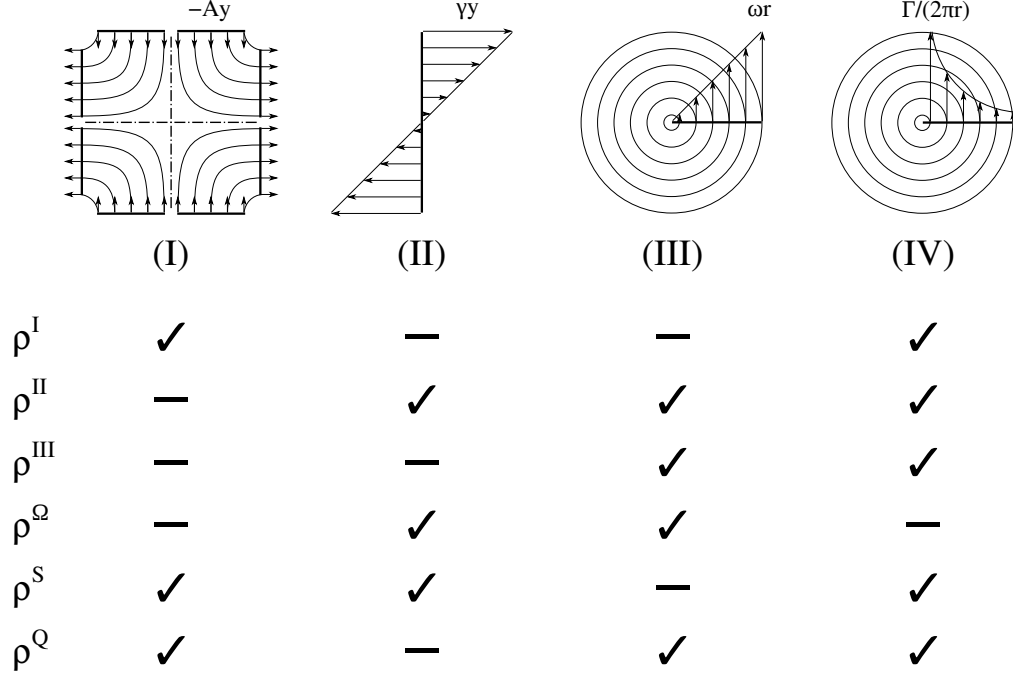


FIG. 6. The schematic of four canonical flows and their effect on various autocovariance functions.

a set of canonical flows. For this purpose, we consider a flow through a corner, a shear flow, a forced vortex, and a free vortex (Fig. 6). The simple form of velocity gradient in these flows allows analytical computation of their corresponding autocovariance functions. Employing these analytical forms to explain the behavior of the autocovariance functions in the HIT flow is by no means conclusive and solely conducted for a qualitative understanding of the observed trends. A more conclusive study would require assessment of the likelihood of exposure of particles to different flow features, which must incorporate the dependence on  $St$ , as well as a more comprehensive range of canonical flows that may occur in a 3-dimensional flow [33].

We first consider flow through a corner or toward a stagnation point, in which  $\mathbf{u} \equiv [x_1, x_2, -2x_3]A$ . In this case,  $u_{i,j}$  is zero for  $i \neq j$ ,  $A$  for  $i = j = 1$  or  $2$ , and  $-2A$  for  $i = j = 3$ . As a result, this canonical flow only contributes to  $\rho^I$ . Although the trajectory of particles varies with the Stokes number, the gradients are uniform in the entire domain, producing  $\rho^I = 2A^2$  that is independent of  $St$ . The independence is relatively

consistent with Fig. 5-(a), in which  $\rho^I(t)$  remains unchanged as  $St$  is increased from  $1/16$  to  $16$ . For  $t \rightarrow \infty$ ,  $u_{i,j}(t')$  becomes uncorrelated with  $u_{i,j}(t + t')$  and hence all functions decay to zero.  $\rho^I$ , however, has the fastest decay rate (shortest integral time scale) among the three functions, indicating that particles travel relatively fast through straining regions of the flow.

Next, we consider a pure shear flow with  $\mathbf{u} \equiv [x_2, 0, 0]\gamma$ . In this case, only  $u_{1,2}$  is nonzero, producing  $\rho^{II} = \gamma^2/6$  and  $\rho^I = \rho^{III} = 0$ . The particle trajectories in this flow are straight lines in  $x_1$  direction and independent of  $St$ . However,  $\rho^{II}(t)$  in Fig. 5-(b) varies as  $St$  changes. Apart from the shear flow,  $\rho^{II}$  is affected by the forced and free vortex flows as well (Fig. 6). As discussed next, the contribution of a forced vortex to  $\rho^{II}$  is  $St$  dependent. Attributing the dependence of  $\rho^{II}$  on  $St$  to the forced vortex, the remaining portion of  $\rho^{II}$  may be attributed to the contribution of regions that are analogous to the shear flow. Comparing the scales of the plots in Fig. 5, the  $St$ -independent portion of  $\rho^{II}$  is notable, suggesting significant exposure of particles to shear in HIT.

The third canonical flow is a forced vortex with  $\mathbf{u} \equiv [-x_2, x_1, 0]\omega$ . For this flow,  $\rho^I = 0$ ,  $\rho^{III} = -\omega^2/3$ , and  $\rho^{II} = \omega^2/3$ . The trajectory of particles in this flow scales as  $r \propto \exp(ct)$ , in which  $r$  is the distance from the vortex core and  $c(\tau, \omega)$  is the solution to  $(\tau c + 1)^2 = \tau c + \tau \omega$ . As a result, the residence time of particles in the core of a forced vortex depends on  $St$ . This dependence and also  $\rho^{II} = -\rho^{III}$  may explain the trend of these two autocovariance functions versus  $St$  at  $t \ll \tau_\eta$  (reproduced in Fig. 7). As  $St$  is increased monotonically,  $\rho^{II}(0) = \overline{u_{1,2}u_{1,2}}$  is decreased and increased while  $\rho^{III}(t = 0) = \overline{u_{1,2}u_{2,1}}$  is increased and decreased with a similar amplitude.  $\overline{u_{1,2}u_{1,2}}$ , which is  $\propto \omega^2$  in a forced vortex, is minimized at  $St = \mathcal{O}(1)$ , confirming the notion that particles in strong clustering regimes of  $St$  are repelled from the vortices.

Lastly, we consider a free vortex with  $\mathbf{u} = [-x_2, x_1, 0]\Gamma/(2\pi r^2)$  in which  $r^2 = x_1^2 + x_2^2 + x_3^2$  is the distance from the center of the vortex. In this flow  $u_{1,2} = u_{2,1} = c \cos(2ct)$  and  $u_{1,1} = c \sin(2ct)$ , in which  $c = \Gamma/(2\pi r^2)$ , producing nonzero  $\rho^I$ ,  $\rho^{II}$ , and  $\rho^{III}$ . Computing the exact value of the autocovariance functions requires finding  $r(t)$ , a nonlinear function that depends on the dimensionless parameter  $\Gamma\tau/r(t = 0)$ . However,  $r$  is almost constant for  $t \ll \tau$  and  $r \propto t^{1/4}$  for  $t \gg \tau$ . Neglecting the dependence of  $r$  on  $t$ , it can

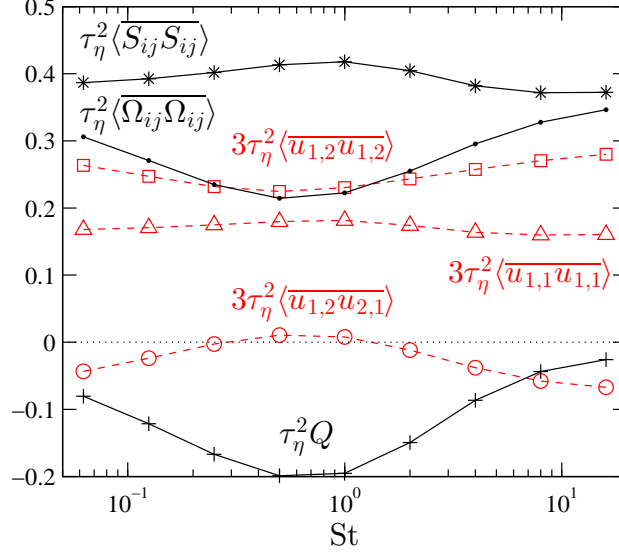


FIG. 7. The ensemble-averaged velocity gradients  $\overline{u_{1,1}u_{1,1}}$  (dashed-triangles),  $\overline{u_{1,2}u_{1,2}}$  (dashed-squares),  $\overline{u_{1,2}u_{2,1}}$  (dashed-circles), rotation-rate (solid-dots), strain-rate (solid-stars), and Q-criterion (solid-plus) as a function of  $St$ . Note  $Q = -\overline{u_{i,j}u_{j,i}} = \|\mathbf{\Omega}\|^2 - \|\mathbf{S}\|^2$  is 2 times the traditional definition of Q-criterion [26], here defined for inertial particles in a Lagrangian framework. Each point in this plot corresponds to an autocorrelation function at zero-time separation, which is the intercept of individual curves in Figs. 5 and 8.

be shown  $\rho^I/2 = \rho^{II} = \rho^{III} = c^2/6 \cos(2ct)$ . This relationship provides an explanation for the decrease and increase of  $\rho^{III}$  in time for  $St \leq 1$  (Fig. 5-(c)). Based on this relationship,  $\rho^{III}(0) - \min_t(\rho^{III}(t)) \propto c^2$  and  $\argmin_t(\rho^{III}(t)) \propto c^{-1}$ . This relation is consistent with the variation of  $\rho^{III}$  for  $t < 5\tau_\eta$  and  $St \leq 1$  in which a larger change in amplitude is associated with a shorter time at which the minimum of  $\rho^{III}$  occurs (Fig. 5-(c)). As oppose to  $\rho^{III}$ ,  $\rho^I$  and  $\rho^{II}$  are apparently unaffected by the free vortices and follow a monotonic trend. An explanation for this behavior is the influence of other canonical flows with larger relative contributions on the latter two functions. To obtain a scale for the relative magnitude of these contributions, note the larger amplitude of  $\rho^I$  and  $\rho^{II}$  in comparison with  $\rho^{III}$  (Fig. 5).

The calculated autocovariance functions can be combined to obtain strain- and rotation-rate autocovariance functions according to Eq. (31) (Figs. 7 and 8). The effect of aforementioned canonical flows on these

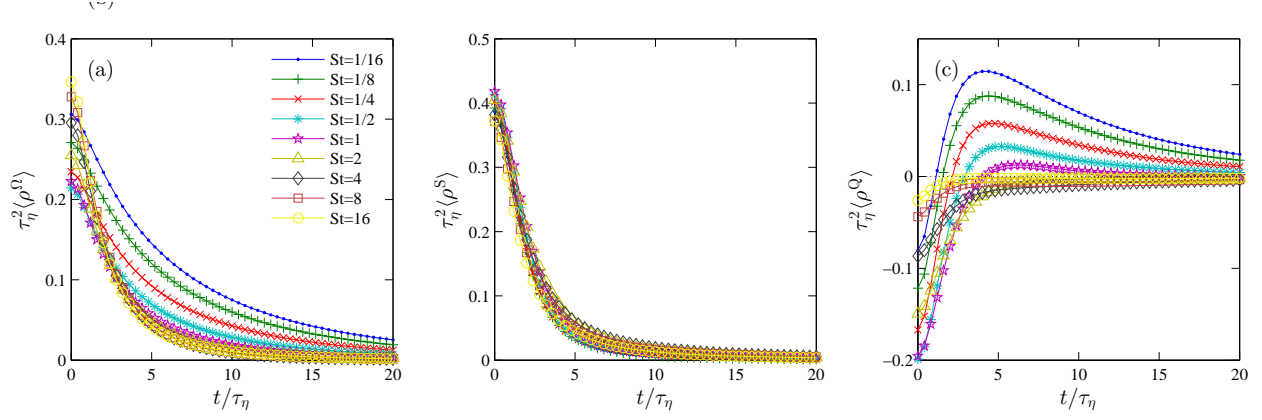


FIG. 8. The ensemble-averaged Lagrangian (a) strain-rate and (b) rotation-rate autocovariance functions and (c) their difference versus time at different Stokes numbers.

functions can also be examined by summing their corresponding contribution on  $\rho^I$ ,  $\rho^{II}$ , and  $\rho^{III}$  (Fig. 6). In Fig. 8-(b),  $\rho^S$  is relatively independent of  $St$  despite the fact that  $\rho^{II}$  and  $\rho^{III}$  vary significantly as  $St$  changes. This independence shows that the variation of  $\rho^{II}$  and  $\rho^{III}$  versus  $St$  are opposite, a behavior that specifically holds in a forced vortex as was shown earlier. These opposite variations, on the other hand, are amplified in  $\rho^\Omega$ , producing a marked dependence on  $St$  (Fig. 8-(a)). Among those considered,  $\rho^\Omega$  is interestingly the only function that is not sensitive to a free vortex (Fig. 6).  $\rho^Q$  captures the effect of all the considered canonical flows but the shear flow. Having  $\rho^Q = 0$  for a shear flow is an expected outcome because  $\mathcal{C}$ , which is a function of  $\tilde{\rho}^Q$ , must be zero in a pure shear flow (no particle clustering is expected in a pure shear flow).

At the limit of very large Stokes numbers, particles are not responsive to the velocity fluctuations and follow a trajectory that is uncorrelated with the flow. As a result, the Lagrangian statistics at this limit converge to the Eulerian statistics, which are by definition obtained from a fixed location in space that is uncorrelated with the flow. Additionally, the Eulerian strain- and rotation-rate autocovariance functions are equal on a periodic domain. Therefore, the Lagrangian strain- and rotation-rate autocovariance functions, i.e.  $\rho^S$  and  $\rho^\Omega$ , converge to the same value at the limit of large  $St$  (Fig. 8). This lead to  $\rho^Q \rightarrow 0$  at the limit of large  $St$ . Moreover, since  $\rho^S$  is relatively independent of the Stokes number, one may conclude that

the trajectory of inertial particles is poorly correlated with the flow strain-rate field. This is not the case, however, with the flow rotation-rate field as  $\rho^\Omega$  varies significantly versus  $St$  (Fig. 8-(a)).  $\rho^Q$  for  $St \leq \mathcal{O}(1)$  undergoes an increasing-decreasing trend in time, which is a consequence of the similar behavior in  $\rho^{III}$ . Attributing this trend to the flow regions that behave similar to a free vortex, one can explain the change in the amplitude and phase of this oscillation as a function of  $St$  by using the expression derived above along with an estimate of the residence time of particles in a free vortex.

Some of the results of this section, specifically those included in Fig. 7, are discussed in more details in [29, 34]. From Fig. 7, the extremum of  $\tau_\eta^2 Q$  is approximately  $-0.2$ , which is consistent with the previously reported  $0.2$  for the maximum of  $\tau_\eta^2(\|\mathbf{S}\|^2 - \|\mathbf{\Omega}\|^2) = -\tau_\eta^2 Q$  [34]. The agreement between the two studies indicates that  $Q$  is fairly insensitive to Reynolds number, as the two studies consider simulations at  $Re_\lambda = 100$  and  $60.5$ . Based on the discrete set of investigated Stokes numbers in these two studies, the Stokes number at which the extremum of  $Q$  occurs is  $0.5$  (present) and  $0.64$  ([34]). A precise assessment of the location of the extremum would require a more refined parameter space.

Taking the Fourier transformation of  $\rho^Q$  in Fig. 8-(c),  $\tilde{\rho}^Q$  is computed and shown in Fig. 9. A biased sampling of strain- and rotation-rate-rich regions of the flow by inertial particles produces a non-zero  $\tilde{\rho}^Q$ . This figure also confirms that particles with  $St < 1$  tend to follow slow vortical features ( $\tilde{\rho}^Q > 0$  at  $\tau_\eta \omega \ll 1$  and  $St < 1$ ), while particles with  $St \gg 1$  experience strain- and rotation-rates equally ( $\tau_\eta \tilde{\rho}^Q \rightarrow 0$  as  $St \rightarrow \infty$ ). Most notably  $\tilde{\rho}^Q$  is negative across all frequencies for  $St \geq \mathcal{O}(1)$ . Computed  $\tilde{\rho}^Q$  is employed in the next section to evaluate and validate present analysis.

## V. NUMERICAL VALIDATION

The objective of this section is to compute the rate of contraction from the analysis that was proposed in Section II and validate it using a direct approach. Hence, we first describe a direct method that provides an accurate estimate of the actual rate of contraction. Additionally, we compute the rate of contraction using present (Eq. (28)) and R-M (Eq. (3)) expressions. Finally, we compare the prediction of these two

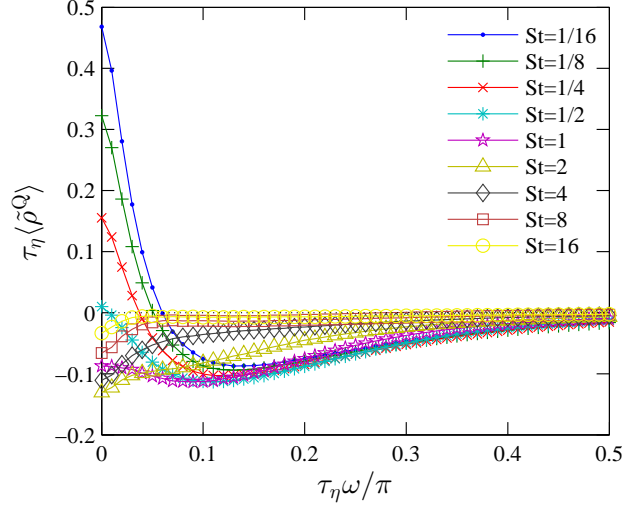


FIG. 9. The Fourier transformation of the autocovariance of the second invariant of the velocity gradient tensor,  $\langle \tilde{\rho}^Q \rangle$ , computed along the trajectory of particles with different Stokes number. Note  $\tau_\eta \langle \tilde{\rho}^Q(\tau_\eta \omega \ll 1) \rangle \propto 1/\text{St}$  as  $\text{St} \rightarrow \infty$ . Error bars (not shown) are of  $\mathcal{O}(10^{-4})$ .

formulations to the direct computations in terms of  $\mathcal{C}$  statistics.

A numerical procedure is devised for direct computation of the contraction rate from the DNS. The direct calculation of  $\mathcal{C}$  sets a baseline, allowing to validate our analysis in a HIT flow. Visually, the direct calculation of  $\mathcal{C}$  involves constructing a cloud by seeding particles randomly distributed on a spherical shell with an infinitesimal diameter. In practice, as clarified below, a cloud can be represented by computing the Lagrangian velocity gradient along trajectory of a single particle. Computing the exponential rate of change of volume of the cloud over time provides a direct estimate of the rate of contraction. Therefore, an ensemble of clouds provides an estimate for  $\langle \mathcal{C} \rangle$ .

Individual particles in the cloud experience an infinitesimally different fluid velocity and as a result follow an infinitesimally different path. This differential change leads to the deformation of the cloud over time. Due to the linear spatial variation of the velocities within the cloud, the deformation is linear and can be represented by a  $3 \times 3$  tensor in 3-dimensions. Applying the deformation tensor to a spherical cloud of

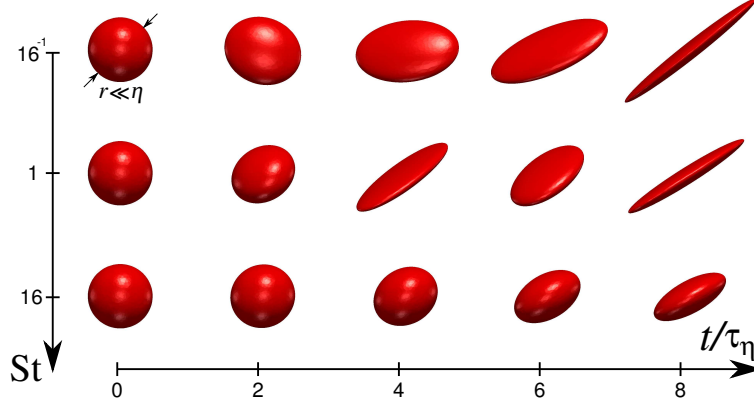


FIG. 10. Deformation of three arbitrary spherical clouds in a HIT flow (particles are not shown). These clouds are constructed using a set of inertial particles initially seeded on a spherical shell. From top to bottom:  $St = 16^{-1}$ , 1, and 16. While the cloud with  $St = 16^{-1}$  deforms significantly, its volume remains within 30% of the initial volume.  $St = 1$  cloud contracts with a two-fold decrease in volume.  $St = 16$  cloud remains almost spherical with a 30% change in volume at  $t = 8\tau_\eta$ .

particles produces an ellipsoid (Fig. 10). The dimensions and directions of the axis of this ellipsoid are directly related to the eigenvalues and eigenvectors of the deformation tensor, respectively. For visualization purposes, the deformation of three arbitrary clouds at  $St = \{1/16, 1, 16\}$  that undergoes a linear deformation is shown in Fig. 10.

In practice, we compute the time evolution of the deformation tensor from direct integration of Eq. (6) along the trajectory of a single particle. The deformation tensor is formed based on the relative position of three virtual particles to a reference particle. Since  $\mathbf{r}$  represents the relative position, three columns of the deformation tensor are formed using  $\mathbf{r}$  associated with the three virtual non-overlapping particles. The time evolution of the deformation tensor is governed by the motion of these particles and thus by Eq. (6). Integrating this equation requires  $u_{i,j}(\mathbf{X}(t); t)$  along the trajectory of the cloud, which is extracted from Section IV in which the Lagrangian autocovariance functions were computed using the same velocity gradients. Provided that the volume of an infinitesimal cloud is equal to the determinant of its corresponding

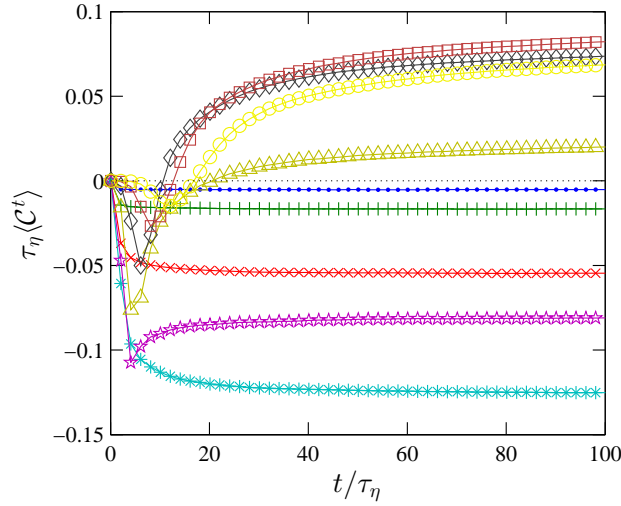


FIG. 11. The ensemble-averaged finite-time contraction rate  $\langle \mathcal{C}^t \rangle$  at different St. To ensure a fully stationary condition when computing  $\mathcal{C}$  from  $\mathcal{C}^t$ , integration is continued to  $2000\tau_\eta$  (only  $t \leq 100\tau_\eta$  is shown here). For symbols, see Fig. 9.

deformation tensor, the time history of the volume of the cloud is calculated, allowing us to compute the finite-time rate of contraction  $\mathcal{C}^t$  based on Eq. (9) (Fig. 11).

Obtaining an accurate estimate of  $\mathcal{C}$ , defined in Eq. (10), requires integrating Eq. (6) till  $t \gg \tau_\eta$ . However, due to the exponential rate of contraction or expansion, the system of equations becomes very stiff at a longer time, producing a nearly singular deformation tensor. Having a stiff system prevents an accurate computation of  $\mathcal{C}$  by limiting  $t$ . To circumvent this issue, we integrate an equivalent system of equations for the normalized rate of change of volume, computed as the ratio of the rate of change of volume by the volume, that remains well-conditioned regardless of the integration period. With this change of variables,  $\mathcal{C}^t$  is computed for the entire sampling period of  $u_{i,j}$ , i.e.  $200\tau_\eta$ . Additionally, the initial condition on the deformation tensor, which is an identity matrix in our computations, affects  $\mathcal{C}^t$  at  $t = 200\tau_\eta$ . To reduce this effect, we repeat the integration for ten cycles, using the solution at the end of each cycle as the initial condition for the next. Hence, integration is continued for  $2000\tau_\eta$  and  $\mathcal{C}$  is set to  $\mathcal{C}^t$  at  $t = 2000\tau_\eta$ . This procedure ensures reported  $\mathcal{C}$  is minimally influenced by the initial condition and is time-independent. By



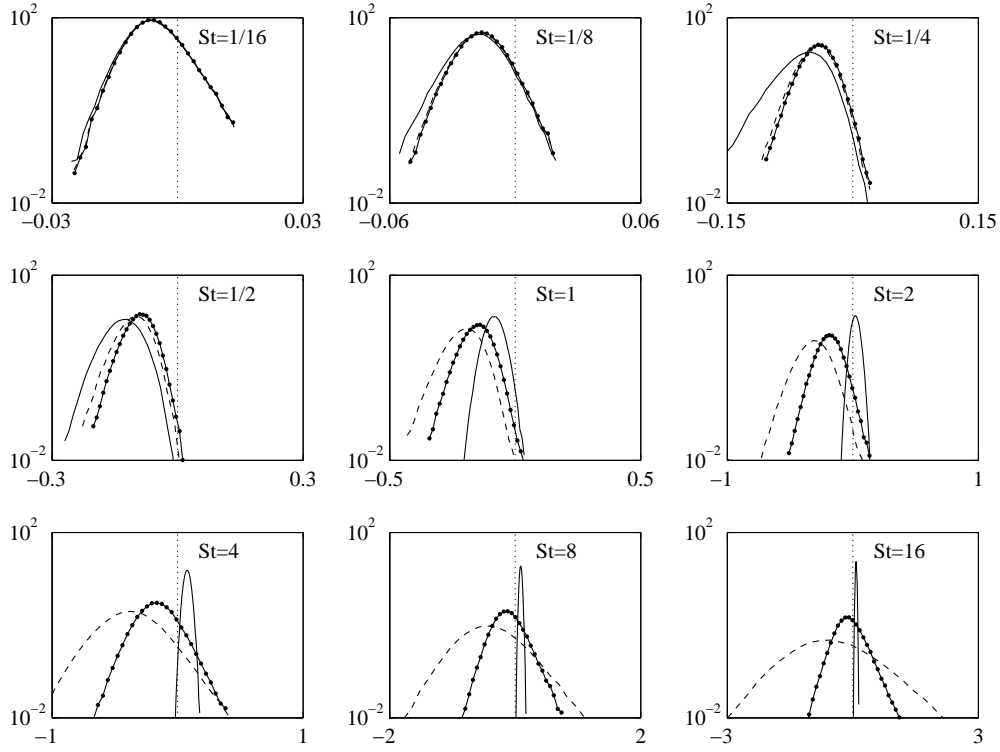


FIG. 12. The PDF of the rate of contraction  $\tau_\eta \mathcal{C}^t$  for different Stokes numbers computed by the direct integration of Eq. (6) (solid), using present analysis or Eq. (28) (solid-dotted), and using R-M or Eq. (3) (dashed). Note that the spread of these PDF varies depending on the sampling period  $t$ , which is  $200\tau_\eta$  in this case.

repeating these computations for all the available particles ( $10^5$  samples that corresponds to  $10^5$  clouds at each St), the PDF of  $\mathcal{C}$  is constructed and shown in Fig. 12.

The results of the direct computation of  $\mathcal{C}$ , described above, along with the theoretically predicted  $\mathcal{C}$  are shown in Fig. 12. The numerical procedure for computing PDFs of the theoretically computed  $\mathcal{C}$  starts from the same data set as the direct computation.  $\rho^Q$  is computed from Eq. (29) for every individual particle, representing a cloud or a sample, using the time history of  $u_{i,j}$  along the particle trajectory.  $Q = \rho^Q(0)$  and  $\tilde{\rho}^Q$  is then computed and substituted in Eqs. (3) and (28), respectively, to obtain one sample point of the corresponding PDFs in Fig. 12. Note the linearity of Eqs. (3) and (28) with respect to  $Q$  and  $\tilde{\rho}^Q$  allows one

to directly compute the mean of these PDFs from the results of Section IV.

Taking the direct calculation of  $\mathcal{C}$  as the reference, present analysis offers an improvement over R-M. As we discussed in the derivation of Eq. (32) and now confirmed by this figure, the prediction of present analysis converges to that of R-M at the limit of small  $St$ . Additionally, the PDF of both analyses collapses with that of the direct calculations, confirming the accuracy of both formulas in the limit of small  $St$ . The accuracy of R-M at this limit has also been shown previously by comparing it against the exact solution of Eq. (6) in straining and vortical flows [34]. In general, the prediction of present analysis is closer to R-M than the reference values. While both analyses are erroneous at large  $St$ , the error of present analysis is smaller than that of R-M. For a closer comparison, the mean of these PDFs is plotted in Fig. 13.

The analytically computed  $\langle \mathcal{C} \rangle$  can be compared to the direct computations at two limits of  $St < 1$  and  $St > 1$ . For  $St < 1$ ,  $\langle \mathcal{C} \rangle < 0$  and contraction dominates expansion. The rate of contraction increase as  $St$  increases, explaining the stronger clustering of particles with  $St = \mathcal{O}(1)$ .  $\tau_{\eta}^{\min} \langle \mathcal{C} \rangle \approx -1/8$ , which occurs at  $St = 1/2$  on the discrete set of investigated  $St$ . In the regime of  $St \ll 1$ ,  $\langle \mathcal{C} \rangle$  follows a power-law with  $-\tau_{\eta} \langle \mathcal{C} \rangle \propto St^{\alpha}$ , in which  $\alpha \approx 1.7$  (inset of Fig. 13). This power-law behavior is well established in the literature for the low Stokes numbers. For a synthetic flow generated from random Fourier modes,  $\alpha$  has been reported to be 2 [16]. This minor difference can be ascribed to the use of a synthetic flow as oppose to HIT in the previous study. The slope of 1.7 in our computation is a result of  $\lim_{St \rightarrow 0} -\tau_{\eta}^2 Q \propto St^{0.7}$  (Fig. 7).

For  $St > 1$ ,  $\langle \mathcal{C} \rangle$  increases and becomes positive, indicating the dominance of expansion over contraction [1, 16]. At a Stokes number between 1 and 2, the mean rate of expansion and contraction become equal. Although  $\langle \mathcal{C} \rangle = 0$  at this  $St$ , individual clouds still experience a significant change in volume over time and particles form distinct clusters (see panels (c) and (d) in Fig. 13). Neither of two analyses captures the positive value of  $\langle \mathcal{C} \rangle$  at large  $St$ . However, present analysis remains bounded by predicting an extremum for  $\langle \mathcal{C} \rangle$  at  $St = \mathcal{O}(1)$  as oppose to the prediction of R-M that grows linearly within the investigated range of  $St$ . For  $St \gg 1$ , present analysis predicts  $\langle \mathcal{C} \rangle \propto St^{-1}$ , which is a result of  $\langle \tilde{\rho}^Q(\tau_{\eta}\omega \ll 1) \rangle \propto St^{-1}$  (Fig. 9). The error in the predictions of present analysis can be primarily attributed to the assumption  $|\lambda\tau| \ll 1$  in

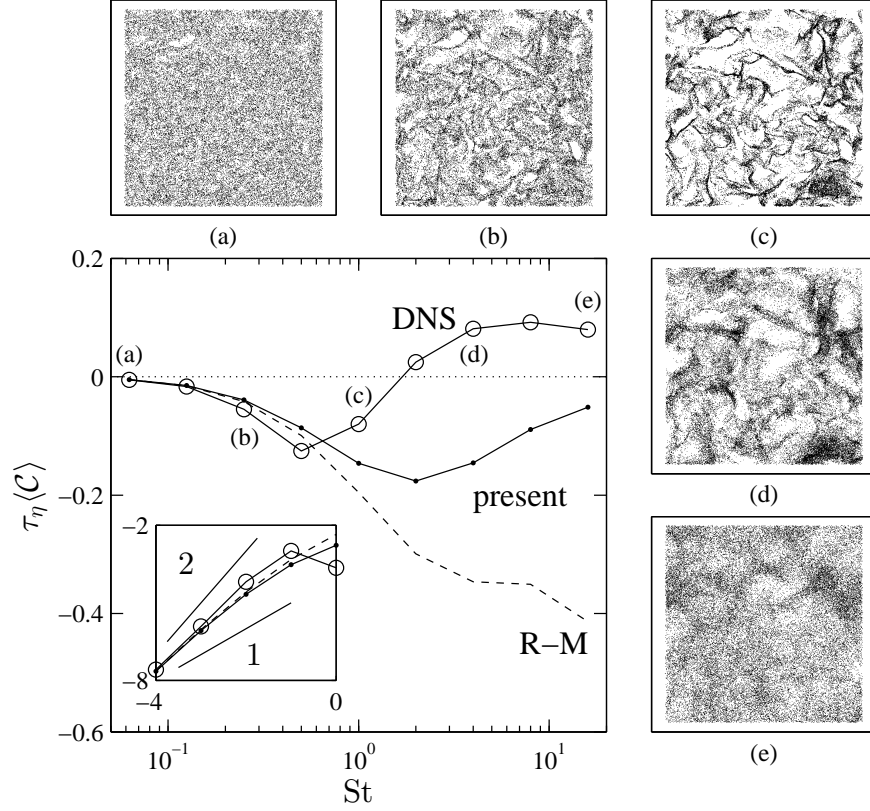


FIG. 13. The theoretically predicted ensemble-averaged rate of contraction  $\langle \mathcal{C} \rangle$  using present analysis that is Eq. (28) (solid-dot) and R-M that is Eq. (3) (dashed) at different  $St$ . The reference quantities (solid-circle) are obtained from the direct computation of  $\langle \mathcal{C} \rangle$ . Inset:  $\log_2(-\mathcal{C})$  versus  $\log_2(St)$  for  $St \leq 1$ . Lines with a slope of 1 and 2 are shown for reference. To visualize clustering, particles are shown in a slab of size  $300\eta \times 300\eta \times 10\eta$  for  $St = 16^{-1}$ , (a);  $4^{-1}$ , (b); 1, (c); 4, (d); 16, (e).

Eq. (12), which is not satisfied well at larger  $St$  ( $|\lambda\tau| > 0.1$  for  $St \geq 4$ ). The effect of this assumption on the accuracy of the predictions can be observed even at  $St = 1/4$ . Considering  $St = 1/4$  case in Fig. 12, the largest deviation from the reference values occurs on the left tail, where  $|\mathcal{C}^t|$  and consequently  $|\lambda\tau|$  is the largest. The location of this discrepancy underscores the importance of  $|\lambda\tau| \ll 1$  assumption in the validity of present analysis. This assumption must be relaxed in the future studies to improve predictions at large

St. Despite this discrepancy, Eq. (28) captures the non-monotonic behavior of  $\langle \mathcal{C} \rangle$  with a maximum rate of contraction 40% larger than that of the direct computations.

As confirmed by the patterns observed in panels (a) and (e) of Fig. 13, particles in the regimes at which  $\mathcal{C} < 0$  and  $\mathcal{C} > 0$  behave differently. In mathematical terms, the volume of the region occupied by particles would increase or decrease in time depending on the sign of  $\mathcal{C}$ . In physical terms, this change of volume has been described as mixing ( $\mathcal{C} > 0$ ) and demixing ( $\mathcal{C} < 0$ ) [16]. For particles that undergo demixing, ridges with high particle concentration is formed from a distribution that is initially homogeneous (Fig. 13-(c)). In a reversed time frame this behavior is the same as injecting a dye in the ridges and observing its diffusion to a homogeneous mixture as time passes. On the other hand, particles with high St undergo mixing with  $\mathcal{C} > 0$ . For an observer who is unable to discern fine scale features of the flow, particle mixing at this limit is similar to mixing of a dye in a turbulent flow as they both appear to lead to a homogenized mixture. However, in the absence of molecular diffusion, there is an important difference between the two processes. While  $\mathcal{C} > 0$  for large St particles,  $\mathcal{C} = 0$  for a dye. When a drop of dye is injected into a turbulent flow with no molecular diffusion, the interface deforms to a very complex and twisted geometry. Nevertheless, the interface remains sharp, and the volume occupied by the dye remains constant in time. This is not the case, however, with the large St particles. If a set of large St particles are introduced into a small enclosed region of a turbulent flow, the volume associated with that region will increase exponentially as the time progresses. In this case, an initially sharp interface will diffuse over time due to the non-uniqueness of particle velocities at a given point in space.

It is important to note that the above description is given for the average behavior of the particles. The clouds of particles with large St experience  $\mathcal{C}^t < 0$  intermittently as they travel through different regions of the flow. The opposite is also true for small St particles. The PDF of  $\mathcal{C}^t$  crosses zero at all Stokes numbers, although not observed clearly in Fig. 12 due to the long sampling period that has reduced the spread of PDFs. Intermittent demixing of large St particles is also confirmed by Fig. 13-(e) that shows regions of higher concentration that are significantly diffused.

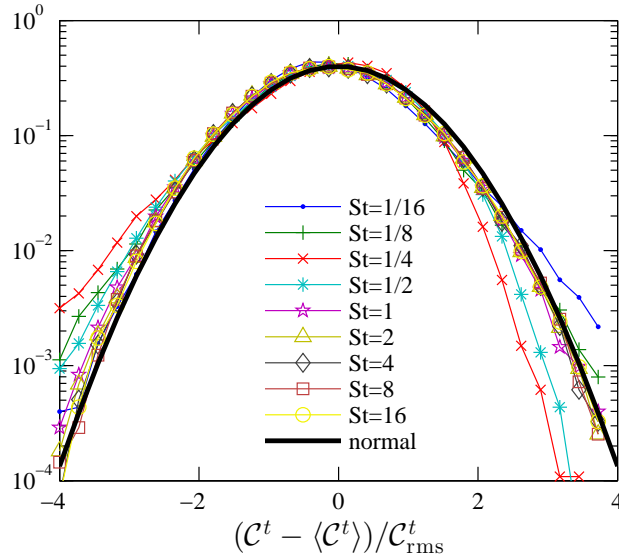


FIG. 14. Standardized PDF of the finite-time rate of contraction  $\mathcal{C}^t$  obtained from the direct integration of Eq. (6) at different  $St$ . The solid line is a Gaussian distribution, shown as a reference.

The PDFs of  $\mathcal{C}^t$  appears to be Gaussian in Fig. 12. To closely examine this observation, all the PDFs obtained from the direct computations are shifted by their mean, normalized by their standard deviation, and plotted in Fig. 14. The standardized PDFs at large  $St$  match well with the parabolic function that represents a Gaussian distribution. For the Stokes numbers close to  $1/4$ , a negative skewness is observed, showing higher incidents of strong contraction events as compared to strong expansion events (Fig. 14). At the smallest  $St$ , the right tail of the PDF is approximately linear, indicative of biased exposure of neutral particles to strong expansion events in HIT. With slight variations, this observation is compatible with the corresponding results obtained from HIT and synthetic flows [16, 20, 35].

The second order statistics of  $\mathcal{C}^t$ , defined as

$$\mathcal{C}_{\text{rms}}^t = \sqrt{\langle (\mathcal{C}^t - \langle \mathcal{C}^t \rangle)^2 \rangle}, \quad (35)$$

is a function that depends on the sampling period  $t$ . For  $t$  larger than the integral time scale of  $\mathcal{C}$ ,  $\mathcal{C}_{\text{rms}}^t$  scales as  $t^{-1/2}$  [20]. Thus,  $\sqrt{\tau_\eta t} \mathcal{C}_{\text{rms}}^t$  is computed as a time-independent quantity and plotted in Fig. 15. This quantity

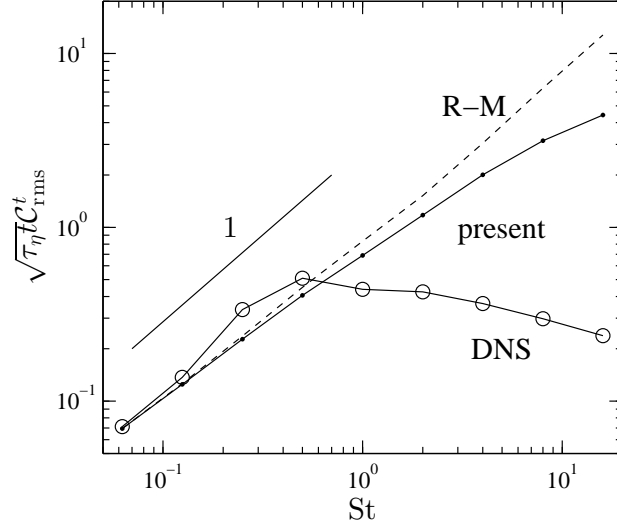


FIG. 15. The standard deviation of the rate of contraction  $\mathcal{C}_{\text{rms}}^t$  using present analysis (solid-dot), R-M (dashed), and the direct computations (solid-circle) as a function of  $St$ . To make values independent of  $t$ ,  $\mathcal{C}_{\text{rms}}^t$  is multiplied by  $\sqrt{t}$ .

is directly related to the compression diffusion coefficient  $D(\infty)$ , defined in [20], via  $\sqrt{\tau_\eta} \mathcal{C}_{\text{rms}}^t = \sqrt{2\tau_\eta D(\infty)}$  and is mainly governed by the turbulence intermittency. Considering the directly computed quantities in Figs. 13 and 15, extremum of  $\mathcal{C}_{\text{rms}}$  and  $\langle \mathcal{C} \rangle$  occurs at the same  $St$ . The prediction accuracy of the two analyses in terms of  $\mathcal{C}_{\text{rms}}$  is analogous to  $\langle \mathcal{C} \rangle$ . Both models agree well with the direct computations at the limit of small  $St$  and deviate from it as  $St$  increases. The error associated with present analysis, however, is slightly smaller than R-M at large  $St$ . The prediction of R-M scales as  $\sqrt{\tau_\eta} \mathcal{C}_{\text{rms}}^t(St) \propto St$ , while present analysis produces slightly smaller values for  $St \geq 1$ .

The non-monotonic prediction of  $\langle \mathcal{C}(St) \rangle$  by our analysis is in agreement with previous investigations that have characterized clustering via other indices, yet consistently finding maximum clustering at  $St = \mathcal{O}(1)$  [3, 10, 14, 28]. The outcome of this study may have implications in developing two-particle models for large-eddy simulation of particle-laden turbulent flows [36] and equilibrium Eulerian method for affordable computation of the particle velocity field [29, 34]. Additionally, one may directly relate the contraction rate

of clouds of particles  $\mathcal{C}$  to

$$d_L = 3 - (\lambda_1 + \lambda_2 + \lambda_3)/\lambda_3 = 3 - \mathcal{C}/\lambda_3, \quad (36)$$

which is the Lyapunov dimension introduced by Kaplan and York [37]. In this equation, which is valid for a 3-dimensional flow, exponents follow a descending order such that  $\lambda_3 < \lambda_2 < \lambda_1$ . Since in 3-dimensions  $\lambda_3 < 0$  [35],  $d_L$  is smaller than the number of spatial dimensions for  $\mathcal{C} < 0$ . At this limit in which particle clusters are fractals,  $d_L$  represents the dimension of the space that contains a homogeneous distribution of particles. By estimating  $\lambda_3$ , one may employ the result of this analysis to estimate  $d_L$ . As we discussed in Section I, this dimension can also be related to the particle concentration field statistics through  $\zeta$ .

## VI. CONCLUSIONS

In summary, we derived an asymptotic solution (Eq. (28)) for the rate of contraction of the cloud of inertial particles, defined as the summation of the Lyapunov exponents in three principal directions, in regimes relevant to particle-laden turbulent flows. The analytical model that we derived predicts a maximum rate of contraction at  $St = \mathcal{O}(1)$  and diminishing rates of contraction as  $St \rightarrow 0$  or  $\infty$ . No adjustable parameters were employed in our model to predict this non-monotonic variation versus the Stokes number. The developed model reproduces R-M, which is a previously established result [25, 29], at small  $St$  and offers a first order correction to it at large  $St$ . Similar to R-M, our analysis accounts for the background flow through  $\tilde{\rho}^Q$ , which is the Fourier transformation of the autocovariance of the second invariant of velocity gradient tensor. We showed  $\tilde{\rho}^Q$ , which is computed along the trajectory of particles, varies significantly versus the Stokes number. The Lagrangian autocovariance functions, which are closely related to  $\tilde{\rho}^Q$ , were computed at different  $St$  for a HIT flow and were analyzed by a set of canonical flows with established behavior. From these results, the first and second order statistics of the rate of contraction was computed using our analysis and a direct numerical approach. Comparing our analysis and the direct computations showed a good agreement between the two at the limit of small  $St$ . For higher  $St$ , despite the fact that the predictions of our analysis are not

in full agreement with the direct computations, it still offers an improvement over R-M. The inaccuracy of present analysis is primarily attributed to the assumption  $|\lambda\tau| \ll 1$ , which breaks down at this regime of  $St$ . Further studies are required to address this discrepancy by analytically characterizing the behavior of particles with  $St \geq \mathcal{O}(1)$  in turbulent flows. The developed analysis reveals the contribution of different time scales in turbulence to the clustering phenomenon via  $\tilde{\rho}^Q(\omega)$ . Lifting the underlying assumptions of present analysis, namely those associated with the contribution of small frequencies in Eqs. (21) and (23) and the slow contraction rate in Eq. (12), warrants future studies. Additionally, the extension of present formulation to compressible and anisotropic turbulent flows remains as a subject of future studies.

## ACKNOWLEDGMENTS

We thank Professors Parviz Moin and John Eaton for fruitful discussions. This work was supported by the United States Department of Energy under the Predictive Science Academic Alliance Program 2 (PSAAP2) at Stanford University.

- 
- [1] Jeremie Bec. Fractal clustering of inertial particles in random flows. *Physics of Fluids*, 15(11):L81–L84, 2003.
  - [2] Enrico Calzavarini, Massimo Cencini, Detlef Lohse, and Federico Toschi. Quantifying turbulence-induced segregation of inertial particles. *Physical Review Letters*, 101(8):084504, 2008.
  - [3] Walter C Reade and Lance R Collins. Effect of preferential concentration on turbulent collision rates. *Physics of Fluids*, 12(10):2530–2540, 2000.
  - [4] John K Eaton and JR Fessler. Preferential concentration of particles by turbulence. *International Journal of Multiphase Flow*, 20:169–209, 1994.
  - [5] S Balachandar and John K Eaton. Turbulent dispersed multiphase flow. *Annual Review of Fluid Mechanics*, 42:111–133, 2010.
  - [6] John R Fessler, Jonathan D Kulick, and John K Eaton. Preferential concentration of heavy particles in a turbulent channel flow. *Physics of Fluids*, 6(11):3742–3749, 1994.



- [7] A Aliseda, Alain Cartellier, F Hainaux, and Juan C Lasheras. Effect of preferential concentration on the settling velocity of heavy particles in homogeneous isotropic turbulence. *Journal of Fluid Mechanics*, 468:77–105, 2002.
- [8] Juan PLC Salazar, Jeremy De Jong, Lujie Cao, Scott H Woodward, Hui Meng, and Lance R Collins. Experimental and numerical investigation of inertial particle clustering in isotropic turbulence. *Journal of Fluid Mechanics*, 600:245–256, 2008.
- [9] Ewe Wei Saw, Raymond A Shaw, Sathyanarayana Ayyalasomayajula, Patrick Y Chuang, and Armann Gylfason. Inertial clustering of particles in high-Reynolds-number turbulence. *Physical review letters*, 100(21):214501, 2008.
- [10] Baidurja Ray and Lance R Collins. Preferential concentration and relative velocity statistics of inertial particles in navier–stokes turbulence with and without filtering. *Journal of Fluid Mechanics*, 680:488–510, 2011.
- [11] Yoshiyuki Tagawa, Julián Martínez Mercado, Vivek N Prakash, Enrico Calzavarini, Chao Sun, and Detlef Lohse. Three-dimensional Lagrangian Voronoi analysis for clustering of particles and bubbles in turbulence. *Journal of Fluid Mechanics*, 693:201–215, 2012.
- [12] Susumu Goto and J.C. Vassilicos. Sweep-stick mechanism of heavy particle clustering in fluid turbulence. *Physical Review Letters*, 100(5):054503, 2008.
- [13] Jérémie Bec. Multifractal concentrations of inertial particles in smooth random flows. *Journal of Fluid Mechanics*, 528:255–277, 2005.
- [14] Jeremie Bec, Luca Biferale, Massimo Cencini, A Lanotte, Stefano Musacchio, and Federico Toschi. Heavy particle concentration in turbulence at dissipative and inertial scales. *Physical Review Letters*, 98(8):084502, 2007.
- [15] Kyle D Squires and John K Eaton. Preferential concentration of particles by turbulence. *Physics of Fluids A: Fluid Dynamics (1989-1993)*, 3(5):1169–1178, 1991.
- [16] Rutger HA Ijzermans, Elena Meneguz, and Michael W Reeks. Segregation of particles in incompressible random flows: singularities, intermittency and random uncorrelated motion. *Journal of Fluid Mechanics*, 653:99–136, 2010.
- [17] H Aref and S Balachandar. Chaotic advection in a Stokes flow. *Physics of Fluids*, 29(11):3515–3521, 1986.
- [18] Romain Monchaux, Mickael Bourgoin, and Alain Cartellier. Analyzing preferential concentration and clustering of inertial particles in turbulence. *International Journal of Multiphase Flow*, 40:1–18, 2012.
- [19] Shawn C Shadden, Francois Lekien, and Jerrold E Marsden. Definition and properties of Lagrangian coherent structures from finite-time Lyapunov exponents in two-dimensional aperiodic flows. *Physica D: Nonlinear*

- Phenomena*, 212(3):271–304, 2005.
- [20] Elena Meneguz and Michael W Reeks. Statistical properties of particle segregation in homogeneous isotropic turbulence. *Journal of Fluid Mechanics*, 686:338–351, 2011.
  - [21] HGE Hentschel and Itamar Procaccia. The infinite number of generalized dimensions of fractals and strange attractors. *Physica D: Nonlinear Phenomena*, 8(3):435–444, 1983.
  - [22] Jérémie Bec, Krzysztof Gawedzki, and Péter Horvai. Multifractal clustering in compressible flows. *Physical review letters*, 92(22):224501, 2004.
  - [23] Michael Wilkinson, Bernhard Mehlig, and Kristian Gustavsson. Correlation dimension of inertial particles in random flows. *EPL (Europhysics Letters)*, 89(5):50002, 2010.
  - [24] Abraham Robinson. On the motion of small particles in a potential field of flow. *Communications on pure and applied mathematics*, 9(1):69–84, 1956.
  - [25] MR Maxey. The gravitational settling of aerosol particles in homogeneous turbulence and random flow fields. *Journal of Fluid Mechanics*, 174:441–465, 1987.
  - [26] Julian CR Hunt, Alan A Wray, and Parviz Moin. Eddies stream, and convergence zones in turbulent flows. *Center for Turbulence Research CTR-S 88*, 1988.
  - [27] Yves Dubief and Franck Delcayre. On coherent-vortex identification in turbulence. *Journal of turbulence*, 1(1):011–011, 2000.
  - [28] Lian-Ping Wang and Martin R Maxey. Settling velocity and concentration distribution of heavy particles in homogeneous isotropic turbulence. *Journal of Fluid Mechanics*, 256:27–68, 1993.
  - [29] Sarma L Rani and S Balachandar. Evaluation of the equilibrium Eulerian approach for the evolution of particle concentration in isotropic turbulence. *International Journal of Multiphase Flow*, 29(12):1793–1816, 2003.
  - [30] E Balkovsky, Gregory Falkovich, and A Fouxon. Intermittent distribution of inertial particles in turbulent flows. *Physical Review Letters*, 86(13):2790, 2001.
  - [31] Carlos Rosales and Charles Meneveau. Linear forcing in numerical simulations of isotropic turbulence: Physical space implementations and convergence properties. *Physics of Fluids*, 17(9):095106, 2005.
  - [32] Maxime Bassenne, Javier Urzay, George I Park, and Parviz Moin. Constant-energetics physical-space forcing methods for improved convergence to homogeneous-isotropic turbulence with application to particle-laden flows. *Physics of Fluids (1994-present)*, 28(3):035114, 2016.

- [33] AE Perry and MS Chong. A description of eddying motions and flow patterns using critical-point concepts. *Annual Review of Fluid Mechanics*, 19(1):125–155, 1987.
- [34] Jim Ferry, Sarma L Rani, and S Balachandar. A locally implicit improvement of the equilibrium Eulerian method. *International journal of multiphase flow*, 29(6):869–891, 2003.
- [35] Jérémie Bec, Luca Biferale, Guido Boffetta, Massimo Cencini, Stefano Musacchio, and Federico Toschi. Lyapunov exponents of heavy particles in turbulence. *Physics of Fluids*, 18(9):091702, 2006.
- [36] Baidurja Ray and Lance R Collins. Investigation of sub-Kolmogorov inertial particle pair dynamics in turbulence using novel satellite particle simulations. *Journal of Fluid Mechanics*, 720:192–211, 2013.
- [37] JL Kaplan and JA Yorke. Functional differential equations and approximation of fixed points. *Lecture notes in mathematics*, 730:228, 1979.